1
2
3
4

Effects of satellite and surface measurements on atmospheric CO assimilations over East Asia in 2015-2020

5 Zhaojun Tang[1], Jiaqi Chen[1], Zhe Jiang[1]*

6

7 [1]School of Earth and Space Sciences, University of Science and Technology of China, Hefei,
8 Anhui, 230026, China.

9

10 *Correspondence to: Zhe Jiang (zhejiang@ustc.edu.cn)

11
12

13 **Abstract**

14 Satellite and surface carbon monoxide (CO) observations have been widely used to investigate

15 the sources and variabilities of atmospheric CO. However, comparative analyses to explore the

16 effects of satellite and surface measurements on atmospheric CO assimilations are still lacking.

17 Here we investigate the evolution of atmospheric CO over E. Asia in 2015-2020, via

18 assimilating CO measurements from the Measurement of Pollution in the Troposphere

19 (MOPITT) and China Ministry of Ecology and Environment (MEE) monitoring network. We

20 find a possible inconsistency by assimilating satellite and surface measurements: the adjusted

21 CO columns are about 3.29, 3.63 and 3.68 x10^{18} molec/cm^2 by assimilating surface CO

22 measurements, in contrast to 2.80-2.93, 3.14-3.25 and 3.09-3.22 x10^{18} molec/cm^2 by

23 assimilating MOPITT CO observations in 2015-2020 over E. China, North China Plain (NCP)

24 and Yangtze River Delta (YRD), respectively. This inconsistency could be associated with

25 possible representation errors due to differences between urban and regional CO backgrounds.

26 Furthermore, assimilations of normalized surface CO measurements (to mitigate the influences

27 of representation errors) indicate declines of CO columns by about 4.0, 4.5, and 4.0 x10^{16}

28 molec/cm^2/y over E. China, South Korea and Japan in 2015-2020, respectively, in contrast to

29 1.7-2.1, 2.1-2.7, and 2.1-2.6 x10^{16} molec/cm^2/y by assimilating MOPITT CO measurements.

30 This discrepancy reflects the different vertical sensitivities of satellite and surface observations

31   in the lower and free troposphere. This work demonstrates the importance to integrate

32   information from satellite and surface measurements to provide a more accurate evaluation for

33   atmospheric CO changes.

34

35   **1. Introduction**

36   Atmospheric CO is one of the most important pollutants and plays a key role in

37   tropospheric chemistry. Sources of atmospheric CO include fossil fuel combustion, biomass

38   burning, and oxidation of hydrocarbons. The importance of atmospheric CO has made it an

39   essential target of global emission controls. Satellite measurements have been used to

40   investigate atmospheric CO changes (Han et al., 2018; Hedelius et al., 2021; Gaubert et al.,

41   2020). Inverse analyses based on satellite measurements further improved our understanding

42   of CO sources. For example, Jiang et al. (2017) constrained global CO emissions in 2001-2015

43   by assimilating MOPITT CO observations. Zheng et al. (2018a) constrained E. Asian CO

44   emissions in 2005-2016 using MOPITT CO observations. Müller et al. (2018) assimilated

45   Infrared Atmospheric Sounding Interferometer (IASI) CO observations to assess the impacts

46   of hydroxyl radical (OH) on derived CO emissions.

47   A major advantage of satellite measurements is the global covered observations. In

48   addition, the pixel-based observations allow convenient comparison with grid-based model

49   simulations. However, the limited vertical resolution implies that the retrieved lower

50   tropospheric CO is affected by free tropospheric CO (Jiang et al., 2013; Buchholz et al., 2017;

51   Hedelius et al., 2021), despite the joint retrieval of near-infrared (NIR) and thermal infrared

52   (TIR) spectral data can enhance the sensitivity to lower tropospheric CO (Worden et al., 2010;

53   Deeter et al., 2017). In contrast to lower tropospheric CO, free tropospheric CO is more

54   susceptible to influences from factors such as long-range transport. Consequently,

55   interpretation of satellite CO measurements requires disentangling of the influences from local

56   and non-local sources.

57   Besides satellite observations, surface in-situ CO measurements have been used to

58   analyze atmospheric CO variabilities (Bouarar et al., 2019; Kong et al., 2020; Squires et al.,

59   2020). There are also recent advances to assess CO sources via assimilating surface CO

60   measurements provided by air quality stations, particularly in China. For example, Peng et al.

61   (2018) assimilated surface CO observations to optimize CO emissions in October 2014. Ma et

62   al. (2019) assimilated surface CO observations to optimize CO emissions in September 2016.

63   Feng et al. (2020) constrained CO emissions in December 2013 and 2017. In contrast to satellite

64   measurements, surface CO observations have rapid responses to local CO emissions.

65   Consequently, the interpretation of surface CO observations is less affected by non-local

66   sources and sinks. However, the sparse distributions of surface stations dimmed the importance

67   of surface CO observations. In addition, it is challenging to match in-situ surface measurements

68   with grid-based model simulations because of noticeable representation errors (Schutgens et

69   al., 2017) and possible uncertainties in the planetary boundary layer (PBL) mixing (Castellanos

70   et al., 2011).

71   To sufficient understand CO variabilities, people may take advantage of information

72   from both satellite and surface measurements. For example, Chen et al. (2020) found

73   decreasing trends of atmospheric CO concentrations from both MOPITT and surface CO

74   measurements over YRD. However, comparative analyses by assimilating satellite and surface

75   CO measurements are still lacking. In this work, we investigate the evolution of atmospheric

76   CO over E. Asia in 2015-2020, via assimilating CO measurements from the MOPITT and MEE

77   surface observations. The objective of this work is to understand the effects of satellite and

78   surface measurements on surface and column CO concentrations in data assimilation system,

79   to explore the methodology of assimilating two types of measurements in data assimilation

80   applications, as well as the impacts of CO emission declines in China on atmospheric CO

Atmospheric
Chemistry
and Physics
Discussions

81   evolution over E. Asia. This paper is organized as follows: In Section 2, we describe the CO

82   observations, GEOS-Chem model, and Kalman Filter approach used in this work. In Section 3,

83   we investigate the performances of satellite and surface measurements in Kalman Filter. Our

84   conclusions follow in Section 4.

85

86   **2. Data and Methodology**

87   **2.1 MOPITT CO measurements**

88   The MOPITT instrument was launched on December 18, 1999 on the NASA/Terra

89   spacecraft. The satellite is in a sun-synchronous polar orbit of 705 km and crosses the equator

90   at 10:30 local time. The instrument makes measurements in a 612 km cross-track scan with a

91   footprint of 22 km x 22 km and provides global coverage every three days. The MOPITT data

92   used here were obtained from the joint retrieval (V8J) of CO from thermal infrared (TIR, 4.7μm)

93   and near-infrared (NIR, 2.3μm) radiances using an optimal estimation approach (Worden et

94   al., 2010; Deeter et al., 2017). The retrieved volume mixing ratios (VMR) are reported as layer

95   averages of 10 pressure levels (surface, 900, 800, 700, 600, 500, 400, 300, 200, and 100 hPa).

96   Following Jiang et al. (2017), we reject MOPITT data with CO column amounts less than

97   5×10^{17} molec/cm^2 and with low cloud observations. Since the NIR radiances measure reflected

98   solar radiation, only daytime data are considered. As shown in Fig. 1a, CO columns provided

99   by MOPITT indicate decreasing trends over E. Asia in 2015-2020, consistent with reported

100   CO variability (Zheng et al., 2018a; Chen et al., 2020; Hedelius et al., 2021).

101

102   **2.2 MEE surface CO measurements**

103   We use MEE surface in-situ CO concentration data (https://quotsoft.net/air/) for the

104   period of 2015-2020. These real-time monitoring stations have the ability to report hourly

105   concentrations of criteria pollutants from over 1670 sites in 2020. Concentrations were reported

106   by the MEE in units of ug/m^3 under standard temperature (273 K) until 31 August 2018. This

Atmospheric
Chemistry
and Physics
Discussions
Open Access

EGU

107   reference state was changed on 1 September 2018 to 298 K. We converted CO concentrations

108   to ppb and rescaled post-August 2018 concentrations to standard temperature (273 K) to keep

109   the consistency in the trend analysis. Fig. 1b shows the trends of surface CO concentrations

110   provided by MEE. There are high-density surface stations in E. China with significant

111   decreasing trends of CO concentrations from 2015 to 2020. The reported data with CO

112   concentrations larger than 6000 ppb are removed in our analysis. In addition, stations absent

113   observations by more than 14 continuous days are filtered to ensure stability in the trend

114   analysis, which affects 17.6% of total stations.

115

116   **2.3 GEOS-Chem model simulations**

117   The GEOS-Chem chemical transport model (http://www.geos-chem.org, version 12-8-1)

118   is driven by assimilated meteorological data of MERRA-2. Our analysis is conducted at a

119   horizontal resolution of nested 0.5°x0.625° and employs the CO-only simulation in GEOS-

120   Chem, which uses archived monthly OH fields from the full chemistry simulation (Fisher et

121   al., 2017). The CO boundary conditions are updated every 3-hour from a global simulation

122   with $4° \times 5°$ resolution. Emissions in GEOS-Chem are computed by the Harvard-NASA

123   Emission Component (HEMCO). Global default anthropogenic emissions are from the CEDS

124   (Community Emissions Data System) (Hoesly et al., 2018). Regional emissions are replaced

125   by MEIC (Multiresolution Emission Inventory for China) in China and MIX in other regions

126   of Asia (Li et al., 2017). The total anthropogenic CO emissions in MEIC inventory are further

127   scaled with linear projections based on Zheng et al. (2018b). Open fire emissions are from the

128   Quick Fire Emissions Dataset (QFED) (Darmenov and da Silva, 2015). The biogenic emissions

129   of VOCs are calculated according to the Model of Emissions of Gases and Aerosols from

130   Nature (MEGAN v2.1) (Guenther et al., 2006).

131

132   **2.4 Kalman Filter approach**

133   We employ the sub-optimal Kalman Filter (Todling and Cohn, 1994) to assimilate

134   MOPITT and surface CO observations. As a brief description of the assimilation algorithm,

135   the forward model (M) predicts CO concentration (x_{at}) at time t:

136    $$x_{at} = M_t x_{t-1} \quad \text{(Eq. 1)}$$

137   The optimized CO concentrations can be expressed as:

138    $$x_t = x_{at} + G_t(y_t - K_t x_{at}) \quad \text{(Eq. 2)}$$

139   where y_t is observation, K_t represents operation operator which projects CO concentrations

140   from the model space to observation space. G_t is the Kalman Filter Gain matrix, which can

141   be described as:

142    $$G_t = S_{at} K_t^T (K_t S_{at} K_t^T + S_\epsilon)^{-1} \quad \text{(Eq. 3)}$$

143   where S_{at} and S_ϵ are model and observation covariance, respectively. The optimized CO

144   concentrations provided by Eq. 2 are then forwarded (hourly) to Eq. 1 for the model simulations

145   in the next time step. We assume fixed model errors (50%). The observation errors include

146   measurement errors and representative errors. The measurement errors are calculated following

147   Feng et al. (2020): $\varepsilon_0 = ermax + 0.005 * \Pi_0$, where $ermax$ is the base error (6 ppb) and

148   Π_0 represents the observed CO concentrations. The representation errors are calculated

149   following Elbern et al. (2007) and Tang et al. (2013): $\varepsilon_r = \gamma \varepsilon_0 \sqrt{\Delta l/L}$, where γ is a scaling

150   factor (0.5), Δl is the model resolution (~56 km in this study), and L represents the range

151   that observation can reflect, which depends on the station type (2 km for urban, 4 km for

152   suburban). Given the measurement error ε_0 and the representative error ε_r the total

153   observation error is defined as $\varepsilon_t = \sqrt{\varepsilon_0^2 + \varepsilon_r^2}$.

154

155   **3. Results and Discussions**

156   **3.1 Kalman Filter assimilating MOPITT CO**

157   We firstly assimilate MOPITT CO data with global simulations (4° × 5° resolution) to

158   optimize E. Asian CO boundary conditions. Same as Jiang et al. (2017), the MOPITT profile

159   and column data are assimilated individually to produce two types of CO boundary conditions.

160   High resolution (0.5°x0.625°) Kalman Filter are performed within E. Asia domain via

161   assimilating MOPITT profile and column data individually, and reading the corresponding CO

162   boundary conditions. As shown in Fig. 2a, we find marked seasonality in surface CO

163   concentrations: about 1200 ppb in winter and 600 ppb in summer. The assimilation of MOPITT

164   CO has small influences on CO concentrations at surface level: the mean surface CO

165   concentrations over E. China increase from 268 ppb to 289-296 ppb in 2015-2020 (Table 1). It

166   could be associated with the limited sensitivity of MOPITT to lower tropospheric CO, as well

167   as the revisit time of satellite measurements, i.e., MOPITT visits an individual model grid every

168   3 days. Thus, the adjustment on surface CO by Kalman Filter can be affected by biased CO

169   emissions in the forward simulations with a 60-minute time step.

170   In contrast to CO at surface level, the Kalman Filter led to marked enhancement of CO

171   columns (Fig. 2b). As shown in Table 1, the modeled CO columns in 2015-2020 were adjusted

172   from about 1.86 to 2.25-2.35 x10^{18} molec/cm^2 over E. China, 2.33 to 2.79-2.89 x10^{18}

173   molec/cm^2 over NCP, and 2.57 to 2.98-3.11 x10^{18} molec/cm^2 over YRD. The difference in the

174   Kalman Filter by assimilating MOPITT column and profile data is small. Fig. 3 further exhibits

175   the CO vertical profiles from model a priori simulations and Kalman Filter. Assimilations of

176   different MOPITT CO data (blue lines) led to similar enhancement of CO abundances, except

177   at high altitudes around 100 hPa. Fig. 4 demonstrates the relative differences between modeled

178   and MOPITT CO columns in 2019. There are pronounced negative biases in the a priori

179   simulations by about 35% (Fig. 4a). By contrast, the differences are dramatically mitigated by

180   assimilating MOPITT CO column data (Fig. 4b), confirming the efficiency of Kalman Filter

181   assimilation.

182   **3.2 Kalman Filter assimilating surface CO**

183   Fig. 2c (black line) shows MEE surface CO observations over NCP in 2019. The blue

Atmospheric
Chemistry
and Physics
Discussions

Open Access

EGU

184   line shows the modeled surface CO concentrations, which are lower than observed CO

185   concentrations. The underestimated surface CO concentrations were reported in recent studies,

186   for example, Peng et al. (2018) found modeled surface CO concentrations by WRF-Chem (752

187    $\mu g/m^3$) are about 40% lower than MEE surface CO (1318 $\mu g/m^3$) in NCP in October 2014.

188   Bouarar et al. (2019) indicated underestimation of surface CO concentrations in WRF-Chem

189   (about 1000 ppb) than surface observations (about 2000 ppb) in Beijing in January 2010. Feng

190   et al. (2020) demonstrated high MEE surface CO in December 2013, i.e., 2.18 mg/m^3 and 1.66

191   mg/m^3 in contrast to 0.86 mg/m^3 and 0.73 mg/m^3 in WRF/CMAQ simulations over NCP and

192   E. China, respectively.

193   We then assimilate MEE surface CO measurements to investigate the impacts on

194   atmospheric CO. In contrast to Kalman Filter by assimilating MOPITT data, the CO boundary

195   conditions here are from a priori simulations. In addition, surface CO measurements are

196   averaged to the GEOS-Chem grids (0.5°x0.625°) before the assimilation. Fig. 2d (orange line)

197   shows the optimized surface CO concentrations in NCP in 2019. The assimilation of surface

198   CO measurements significantly improved the agreement between observations and model

199   simulations. As shown in Table 1, the modeled surface CO concentrations in 2015-2020 are

200   increased from 268 to 430 ppb over E. China, 445 to 630 ppb over NCP and 418 to 599 ppb

201   over YRD. The correlations between modeled and observed surface CO are enhanced from

202   0.707 to 0.934 over NCP in 2019. The enhancement of surface CO concentrations due to

203   assimilating surface CO measurements have been reported in recent studies. For example, Peng

204   et al. (2018) demonstrated enhancement of surface CO from 752 $\mu g/m^3$ to 1418 $\mu g/m^3$ in NCP

205   in October 2014. Feng et al. (2020) exhibited enhancement of surface CO from 0.73 mg/m^3 to

206   1.62 mg/m^3 in December 2013 over E. China.

207   **3.3 Discrepancy in CO columns by assimilating satellite and surface CO**

208   As shown in Fig. 3, the modeled CO profile by assimilating MEE surface CO (red solid

209   line) is higher than MOPITT-based CO concentrations (blue lines), particularly, in the lower

210   troposphere. It indicates a possible discrepancy in the adjusted CO concentrations by

211   assimilating satellite and surface observations. We thus, sample satellite- and model-based CO

212   concentrations at the locations of MEE stations to evaluate their consistency in data

213   assimilations (Table 2). Like Fig. 3, the adjusted surface CO concentrations by assimilating

214   MEE CO measurements are higher than those by assimilating MOPITT data in 2015-2020: 631

215   and 417-428 ppb over E. China; 806 and 627-639 ppb over NCP; 657 and 500-509 ppb over

216   YRD. In addition, the adjusted CO columns by assimilating MEE CO measurements are higher

217   than those by assimilating MOPITT data in 2015-2020: 3.29 and 2.80-2.93 x10^{18} molec/cm^2

218   over E. China; 3.63 and 3.14-3.25 x10^{18} molec/cm^2 over NCP; 3.68 and 3.09-3.22 x10^{18}

219   molec/cm^2 over YRD.

220   MOPITT CO retrievals have been sufficiently evaluated, for example, Deeter et al.

221   (2017) indicated that the bias in MOPITT CO column data is about 3% in respective to NOAA

222   flask measurements. Furthermore, as shown in Fig. 4a, the modeled CO columns from the

223   boundary conditions are biased low by about 40%, which was not removed when assimilating

224   MEE surface CO. The higher CO columns by assimilating MEE CO measurements thus

225   indicate possible overestimated enhancements on free tropospheric CO. Similarly, Feng et al.

226   (2020) suggested a 186% enhancement of CO emissions over E. China via assimilating surface

227   CO measurements. By contrast, the MOPITT-based CO emission estimates are comparable

228   with a priori emissions in China (Elguindi et al., 2020).

229   Fig. 1c-d exhibit the modeled and observed surface CO, as well as the ratios between

230   observed and modeled surface CO in 2019. The ratios are about 1.5 over high polluted areas

231   such as NCP and 2-6 over low polluted areas (Fig. 1d). Because most MEE stations are urban

232   air quality sites, the regional discrepancy in the ratios reveals possible influences from

Atmospheric
Chemistry
and Physics
Discussions

Open Access

EGU

233 representation error, i.e., the regional CO backgrounds are lower than observations from urban

234 stations, and the influences are stronger over low polluted areas. Despite representation errors

235 have been considered in the covariance matrix in the Kalman Filter (Section 2.4), it seems that

236 the mitigation of representation errors is limited. It is not surprising because the covariance

237 matrix is supposed to contain random errors with Gaussian distribution, whereas representation

238 errors due to differences between urban and regional backgrounds are systematic biases. In

239 addition, insufficient parameterized processes such as PBL mixing can further contribute to the

240 underestimation of modeled surface CO concentrations (Castellanos et al., 2011).

241 **3.4 Kalman Filter assimilating normalized surface CO**

242 The possible systematic biases imply it may not be a good idea to assimilate surface CO

243 measurements to optimize free tropospheric CO directly. Alternatively, account for the good

244 capability of models to capture the observed CO variabilities, we can consider scaling surface

245 CO measurements using the ratios between observations and models. The MEE surface CO

246 measurements will be scaled using the ratios shown in Fig. 1d in the following discussions.

247 The actual effect of this adjustment is normalizing modeled and observed surface CO

248 concentrations in 2019, and hence, Kalman Filter, by assimilating the normalized surface CO

249 measurements can reflect the variabilities (i.e., trends) instead of magnitudes of CO

250 concentrations. It should be noted that the ratios are expected to be affected by interannual

251 variabilities of meteorological conditions as well as possible land usage changes. We assume

252 small influences from meteorological condition variabilities because of the stable PBL height

253 in E. China in 2013-2017 (Wang et al., 2020). The land usage changes are supposed to be

254 insignificant due to the limited studied period (i.e., 2015-2020).

255 Fig. 2e (orange line) shows surface CO concentrations in NCP in 2019 by assimilating

256 normalized surface CO measurements. The magnitudes of model a priori (blue line) and

257 Kalman Filter (orange line) are consistent in Fig. 2g due to the normalization of surface CO

Atmospheric
Chemistry
and Physics
Discussions

258 measurements. As shown in Table 2, the adjusted surface and column CO concentrations by

259 assimilating normalized MEE CO measurements are closer to the a priori simulations in 2015-

260 2020. The correlation between modeled and observed surface CO is 0.865 over NCP in 2019,

261 which is lower than the correlation by assimilating raw surface CO measurements.

262 Furthermore, we performed sensitivity assimilation to evaluate the effects of MOPITT pass

263 time by only assimilating MEE CO measurements in the morning. As shown in Table 2, the

264 assimilation of morning data led to lower surface and column CO concentrations, and thus, the

265 discrepancy in the CO columns (Section 3.3) is not driven by different temporal resolutions

266 between satellite and surface CO observations.

267 **3.5 Evolution of atmospheric CO over E. Asia in 2015-2020**

268 Here we expand our analysis to investigate the evolution of atmospheric CO over E. Asia

269 in 2015-2020. As shown in Fig. 5a, Kalman Filter, by assimilating raw surface CO

270 measurements reveal wide declines of surface CO concentrations over E. China. The declines

271 of surface CO resulted in decreases of CO columns (Fig. 5b, via assimilating normalized

272 surface CO measurements), by about 4.0, 4.5, and 4.0 x10^{16} molec/cm^2/y in 2015-2020 (Table

273 1) over E. China, South Korea and Japan, respectively. By contrast, the decreasing trends in

274 the MOPITT-based assimilations (Fig. 5c-d) are weaker: 1.7-2.1, 2.1-2.7, and 2.1-2.6 x10^{16}

275 molec/cm^2/y in 2015-2020 (Table 1) over E. China, South Korea and Japan, respectively. Fig.

276 5e further demonstrates the trends of CO columns by assimilating both MOPITT CO column

277 and normalized surface CO measurements: the decreasing trends are about 4.1, 4.6, and 4.0

278 x10^{16} molec/cm^2/y in 2015-2020 (Table 1) over E. China, South Korea and Japan, respectively.

279 As shown in Fig. 6, the a priori simulations with fixed anthropogenic CO emissions in

280 2010 (black lines) predict stable surface CO concentrations in 2015-2020. By contrast, Kalman

281 Filter by assimilating raw surface CO measurements (red solid lines) demonstrates declines of

282 surface CO concentrations by about 62.2, 21.0 and 30.6 ppb/y over NCP, YRD and E. China,

283   respectively. The difference between the a priori simulations (black lines) and assimilations

284   (red solid lines) indicates the impacts of successful CO emission controls in China. In addition,

285   Kalman Filter by assimilating normalized surface CO measurements (red dashed lines)

286   indicates declines of surface CO concentrations by about 51.0, 18.2 and 18.6 ppb/y over NCP,

287   YRD and E. China, respectively. While the normalized CO measurements are supposed to

288   provide a better representation of atmospheric CO in the free troposphere, Kalman Filter by

289   assimilating raw CO measurements (red solid lines) is closer to real urban CO concentrations

290   at surface level.

291   Finally, we analyze the interannual variabilities of CO columns by assimilating MOPITT

292   and surface CO measurements. As shown in Fig. 7, Kalman Filter by assimilating normalized

293   surface CO measurements (red dashed lines) demonstrates declines of CO columns by about

294   9.1, 6.0 and 4.0 $x10^{16}$ molec/cm^2/y in 2015-2020 over NCP, YRD and E. China, respectively.

295   Kalman Filter by assimilating raw surface CO measurements (red solid lines) led to

296   overestimated CO columns. Kalman Filter by assimilating MOPITT CO columns (blue lines)

297   exhibit smaller changes of CO columns: 2.3-2.9, 1.7-2.0 and 1.7-2.1 $x10^{16}$ molec/cm^2/y in

298   2015-2020 (Table 1) over NCP, YRD and E. China, respectively. Kalman Filter by assimilating

299   both MOPITT CO column and normalized surface CO measurements (purple lines) exhibits

300   decreasing trends of CO columns by about 9.3, 6.0 and 4.1 $x10^{16}$ molec/cm^2/y in 2015-2020

301   over NCP, YRD and E. China, respectively.

302   **4. Conclusion**

303   A comparative analysis is provided in this work to explore the effects of satellite and

304   surface measurements on atmospheric CO assimilations over E. Asia in 2015-2020. We find a

305   possible inconsistency by assimilating satellite and surface CO measurements: the adjusted CO

306   columns are about 3.29, 3.63 and 3.68 $x10^{18}$ molec/cm^2 by assimilating surface CO

307   measurements, in contrast to 2.80-2.93, 3.14-3.25 and 3.09-3.22 $x10^{18}$ molec/cm^2 by

308   assimilating MOPITT CO observations in 2015-2020 over E. China, NCP and YRD,

309   respectively. This difference is larger than the reported uncertainties in MOPITT CO columns

310   (Deeter et al., 2017) and similar to the reported discrepancy in the derived CO emissions based

311   on MOPITT and surface CO measurements (Elguindi et al., 2020; Feng et al., 2020).

312   Furthermore, we find large regional discrepancies in the ratios between observed and modeled

313   surface CO: about 1.5 over high polluted areas such as NCP and 2-6 over low polluted areas

314   (Fig. 1d). The different effects of satellite and surface measurements on atmospheric CO

315   assimilations could thus, be partially associated with representation errors due to differences

316   between urban and regional CO backgrounds, which cannot be effectively contained via

317   adjusting covariance matrix in the assimilations.

318   Assimilations of raw surface CO measurements indicate declines of surface CO

319   concentrations by about 62.2, 21.0 and 30.6 ppb/y over NCP, YRD and E. China in 2015-2020.

320   Assimilations of normalized surface CO measurements further indicate declines of CO

321   columns by about 4.0, 4.5, and 4.0 x10^{16} molec/cm^2/y over E. China, South Korea and Japan

322   in 2015-2020, respectively. It demonstrates the important impacts of CO emission controls in

323   China on E. Asian atmospheric CO evolution. By contrast, assimilations of MOPITT CO

324   measurements suggest small trends in CO columns: 1.7-2.1, 2.1-2.7, and 2.1-2.6 x10^{16}

325   molec/cm^2/y over E. China, South Korea and Japan in 2015-2020, respectively. This

326   discrepancy reflects the different vertical sensitivities of satellite and surface observations to

327   CO concentrations in the lower and free troposphere. More efforts to integrate information

328   from satellite and surface CO measurements are expected to provide more accurate evaluation

329   for atmospheric CO changes.

330

331   **Data availability:** The MEE CO data can be downloaded from https://quotsoft.net/air/. The

332   MOPITT CO data can be downloaded from https://asdc.larc.nasa.gov/data/MOPITT/. The

333   GEOS-Chem   model   (version   12.8.1)   can   be   downloaded   from

334   http://wiki.seas.harvard.edu/geos-chem/index.php/GEOS-Chem_12#12.8.1.

335

344

345   **Figure Legends**

346   **Table 1.** Averages and trends of surface and column CO concentrations in 2015-2020. The

347   domain definitions are shown in Fig. 1a.

348

349   **Table 2.** Averages and trends of surface and column CO concentrations in 2015-2020, sampled

350   at the locations of MEE stations. The domain definitions are shown in Fig. 1a.

351

352   **Figure 1.** (A) Trends of MOPITT CO columns in 2015-2020 with unit 10^{18} molec/cm^2/y; (B)

353   Trends of MEE surface CO concentrations in 2015-2020 with unit ppb/y; (C) Modeled

354   (contour) and observed (dotted) surface CO concentrations in 2019 with unit ppb; (D) Ratios

355   between observed and modeled surface CO concentrations in 2019. The black boxes in panel

356   A define the domains (land only) of E. China, NCP, YRD, South Korea and Japan. The areas

357   outside of China are excluded in the E. China domain.

358

359   **Figure 2.** (A) surface CO concentrations over NCP in 2019 from a priori simulation and

360   Kalman Filter by assimilating MOPITT CO; (B) same as panel a, but for CO columns; (C)

361 surface CO concentrations from a priori simulation and MEE observations; (D) surface CO

362 concentrations from a priori simulation, MEE observations and Kalman Filter by assimilating

363 MEE CO; (E) surface CO concentrations from a priori simulation, MEE observations and

364 Kalman Filter by assimilating normalized MEE CO.

365

366 **Figure 3.** CO profiles over NCP in 2019 from a priori simulations (black line), Kalman Filter

367 by assimilating MOPITT CO (column: blue solid line; profile: blue dashed line) and MEE CO

368 (raw data: red solid line; normalized data: red dashed line).

369

370 **Figure 4.** (A) relative difference between a priori simulation and MOPITT in 2019, calculated

371 by (Model - MOPITT)/MOPITT; (B) same as panel A, but with Kalman Filter by assimilating

372 MOPITT CO column data; (C) same as panel A, but with Kalman Filter by assimilating

373 MOPITT CO profile data.

374

375 **Figure 5.** Trends of surface CO concentrations in 2015-2020 by assimilating raw MEE CO (A)

376 and trends of CO columns in 2015-2020 by assimilating (B) normalized MEE CO; (C)

377 MOPITT CO column data; (D) MOPITT CO profile data; (E) normalized MEE CO + MOPITT

378 CO column data.

379

380 **Figure 6.** (A-C) Surface CO concentrations in 2015-2019 from a priori simulations (black line),

381 Kalman Filter by assimilating raw (red solid line) and normalized (red dashed line) MEE CO.

382 (D-F) same as panels a-c, but sampled at the locations of MEE stations.

383

384 **Figure 7.** (A-C) CO columns in 2015-2020 from a priori simulations (black line), Kalman

385 Filter by assimilating MOPITT CO columns (blue line), MEE CO (raw data: red solid line;

386 normalized data: red dashed line) and MOPITT CO column + normalized MEE CO (purple

387 line). (D-F) same as panels a-c, but sampled at the locations of MEE stations.

388

389 **References**

390 Bouarar, I., Brasseur, G., Petersen, K., Granier, C., Fan, Q., Wang, X., Wang, L., Ji, D., Liu,

391 Z., Xie, Y., Gao, W., and Elguindi, N.: Influence of anthropogenic emission inventories on

392 simulations of air quality in China during winter and summer 2010, Atmos Environ, 198, 236-

393 256, 10.1016/j.atmosenv.2018.10.043, 2019.

394 Buchholz, R. R., Deeter, M. N., Worden, H. M., Gille, J., Edwards, D. P., Hannigan, J. W.,
395 Jones, N. B., Paton-Walsh, C., Griffith, D. W. T., Smale, D., Robinson, J., Strong, K.,
396 Conway, S., Sussmann, R., Hase, F., Blumenstock, T., Mahieu, E., and Langerock, B.:
397 Validation of MOPITT carbon monoxide using ground-based Fourier transform infrared
398 spectrometer data from NDACC, Atmos Meas Tech, 10, 1927-1956, 10.5194/amt-10-1927-
399 2017, 2017.
400 Castellanos, P., Marufu, L. T., Doddridge, B. G., Taubman, B. F., Schwab, J. J., Hains, J. C.,
401 Ehrman, S. H., and Dickerson, R. R.: Ozone, oxides of nitrogen, and carbon monoxide during
402 pollution events over the eastern United States: An evaluation of emissions and vertical
403 mixing, Journal of Geophysical Research, 116, 10.1029/2010jd014540, 2011.
404 Chen, Y., Ma, Q., Lin, W., Xu, X., Yao, J., and Gao, W.: Measurement report: Long-term
405 variations in carbon monoxide at a background station in China's Yangtze River Delta region,
406 Atmos Chem Phys, 20, 15969-15982, 10.5194/acp-20-15969-2020, 2020.
407 The Quick Fire Emissions Dataset (QFED): Documentation of versions 2.1, 2.2 and 2.4, NASA
408 Technical Report Series on Global Modeling and Data Assimilation NASA TM-2015-
409 104606, Volume 38: http://gmao.gsfc.nasa.gov/pubs/docs/Darmenov796.pdf, 2015.
410 Deeter, M. N., Edwards, D. P., Francis, G. L., Gille, J. C., Martínez-Alonso, S., Worden, H.
411 M., and Sweeney, C.: A climate-scale satellite record for carbon monoxide: the MOPITT
412 Version 7 product, Atmos Meas Tech, 10, 2533-2555, 10.5194/amt-10-2533-2017, 2017.
413 Elbern, H., Strunk, A., Schmidt, H., and Talagrand, O.: Emission rate and chemical state
414 estimation by 4-dimensional variational inversion, Atmos Chem Phys, 7, 3749-3769,
415 10.5194/acp-7-3749-2007, 2007.
416 Elguindi, N., Granier, C., Stavrakou, T., Darras, S., Bauwens, M., Cao, H., Chen, C., Denier
417 van der Gon, H. A. C., Dubovik, O., Fu, T. M., Henze, D. K., Jiang, Z., Keita, S., Kuenen, J.
418 J. P., Kurokawa, J., Liousse, C., Miyazaki, K., Müller, J. F., Qu, Z., Solmon, F., and Zheng,
419 B.: Intercomparison of Magnitudes and Trends in Anthropogenic Surface Emissions From
420 Bottom‐Up Inventories, Top‐Down Estimates, and Emission Scenarios, Earth's Future, 8,
421 10.1029/2020ef001520, 2020.
422 Feng, S., Jiang, F., Wu, Z., Wang, H., Ju, W., and Wang, H.: CO Emissions Inferred From
423 Surface CO Observations Over China in December 2013 and 2017, J Geophys Res-Atmos,
424 125, 10.1029/2019jd031808, 2020.
425 Fisher, J. A., Murray, L. T., Jones, D. B. A., and Deutscher, N. M.: Improved method for linear
426 carbon monoxide simulation and source attribution in atmospheric chemistry models
427 illustrated using GEOS-Chem v9, Geosci Model Dev, 10, 4129-4144, 10.5194/gmd-10-4129-
428 2017, 2017.
429 Gaubert, B., Emmons, L. K., Raeder, K., Tilmes, S., Miyazaki, K., Arellano, A. F., Jr.,
430 Elguindi, N., Granier, C., Tang, W., Barre, J., Worden, H. M., Buchholz, R. R., Edwards, D.
431 P., Franke, P., Anderson, J. L., Saunois, M., Schroeder, J., Woo, J. H., Simpson, I. J., Blake,
432 D. R., Meinardi, S., Wennberg, P. O., Crounse, J., Teng, A., Kim, M., Dickerson, R. R., He,
433 H., Ren, X., Pusede, S. E., and Diskin, G. S.: Correcting model biases of CO in East Asia:
434 impact on oxidant distributions during KORUS-AQ, Atmos Chem Phys, 20, 14617-14647,
435 10.5194/acp-20-14617-2020, 2020.

436 Guenther, A., Karl, T., Harley, P., Wiedinmyer, C., Palmer, P. I., and Geron, C.: Estimates of
437   global terrestrial isoprene emissions using MEGAN (Model of Emissions of Gases and
438   Aerosols from Nature), Atmos Chem Phys, 6, 3181-3210, 10.5194/acp-6-3181-2006, 2006.
439 Han, H., Liu, J., Yuan, H., Jiang, F., Zhu, Y., Wu, Y., Wang, T., and Zhuang, B.: Impacts of
440   Synoptic Weather Patterns and their Persistency on Free Tropospheric Carbon Monoxide
441   Concentrations and Outflow in Eastern China, J Geophys Res-Atmos, 123, 7024-7046,
442   10.1029/2017jd028172, 2018.
443 Hedelius, J. K., Toon, G. C., Buchholz, R. R., Iraci, L. T., Podolske, J. R., Roehl, C. M.,
444   Wennberg, P. O., Worden, H. M., and Wunch, D.: Regional and Urban Column CO Trends
445   and Anomalies as Observed by MOPITT Over 16 Years, J Geophys Res-Atmos, 126,
446   10.1029/2020jd033967, 2021.
447 Hoesly, R. M., Smith, S. J., Feng, L., Klimont, Z., Janssens-Maenhout, G., Pitkanen, T.,
448   Seibert, J. J., Vu, L., Andres, R. J., Bolt, R. M., Bond, T. C., Dawidowski, L., Kholod, N.,
449   Kurokawa, J.-i., Li, M., Liu, L., Lu, Z., Moura, M. C. P., O'Rourke, P. R., and Zhang, Q.:
450   Historical (1750–2014) anthropogenic emissions of reactive gases and aerosols from the
451   Community Emissions Data System (CEDS), Geosci Model Dev, 11, 369-408, 10.5194/gmd-
452   11-369-2018, 2018.
453 Jiang, Z., Jones, D. B. A., Worden, H. M., Deeter, M. N., Henze, D. K., Worden, J., Bowman,
454   K. W., Brenninkmeijer, C. A. M., and Schuck, T. J.: Impact of model errors in convective
455   transport on CO source estimates inferred from MOPITT CO retrievals, J Geophys Res-
456   Atmos, 118, 2073-2083, 10.1002/jgrd.50216, 2013.
457 Jiang, Z., Worden, J. R., Worden, H., Deeter, M., Jones, D. B. A., Arellano, A. F., and Henze,
458   D. K.: A 15-year record of CO emissions constrained by MOPITT CO observations, Atmos
459   Chem Phys, 17, 4565-4583, 10.5194/acp-17-4565-2017, 2017.
460 Kong, L., Tang, X., Zhu, J., Wang, Z., Fu, J. S., Wang, X., Itahashi, S., Yamaji, K., Nagashima,
461   T., Lee, H.-J., Kim, C.-H., Lin, C.-Y., Chen, L., Zhang, M., Tao, Z., Li, J., Kajino, M., Liao,
462   H., Wang, Z., Sudo, K., Wang, Y., Pan, Y., Tang, G., Li, M., Wu, Q., Ge, B., and Carmichael,
463   G. R.: Evaluation and uncertainty investigation of the NO_2, CO and NH_3 modeling over China
464   under the framework of MICS-Asia III, Atmos Chem Phys, 20, 181-202, 10.5194/acp-20-
465   181-2020, 2020.
466 Li, M., Zhang, Q., Kurokawa, J.-i., Woo, J.-H., He, K., Lu, Z., Ohara, T., Song, Y., Streets, D.
467   G., Carmichael, G. R., Cheng, Y., Hong, C., Huo, H., Jiang, X., Kang, S., Liu, F., Su, H., and
468   Zheng, B.: MIX: a mosaic Asian anthropogenic emission inventory under the international
469   collaboration framework of the MICS-Asia and HTAP, Atmos Chem Phys, 17, 935-963,
470   10.5194/acp-17-935-2017, 2017.
471 Ma, C., Wang, T., Mizzi, A. P., Anderson, J. L., Zhuang, B., Xie, M., and Wu, R.:
472   Multiconstituent Data Assimilation With WRF‐Chem/DART: Potential for Adjusting
473   Anthropogenic Emissions and Improving Air Quality Forecasts Over Eastern China, J
474   Geophys Res-Atmos, 10.1029/2019jd030421, 2019.
475 Müller, J. F., Stavrakou, T., Bauwens, M., George, M., Hurtmans, D., Coheur, P. F., Clerbaux,
476   C., and Sweeney, C.: Top‐Down CO Emissions Based On IASI Observations and

477   Hemispheric Constraints on OH Levels, Geophys Res Lett, 45, 1621-1629,
478   10.1002/2017gl076697, 2018.
479   Peng, Z., Lei, L., Liu, Z., Sun, J., Ding, A., Ban, J., Chen, D., Kou, X., and Chu, K.: The impact
480   of multi-species surface chemical observation assimilation on air quality forecasts in China,
481   Atmos Chem Phys, 18, 17387-17404, 10.5194/acp-18-17387-2018, 2018.
482   Schutgens, N., Tsyro, S., Gryspeerdt, E., Goto, D., Weigum, N., Schulz, M., and Stier, P.: On
483   the spatio-temporal representativeness of observations, Atmos Chem Phys, 17, 9761-9780,
484   10.5194/acp-17-9761-2017, 2017.
485   Squires, F. A., Nemitz, E., Langford, B., Wild, O., Drysdale, W. S., Acton, W. J. F., Fu, P.,
486   Grimmond, C. S. B., Hamilton, J. F., Hewitt, C. N., Hollaway, M., Kotthaus, S., Lee, J.,
487   Metzger, S., Pingintha-Durden, N., Shaw, M., Vaughan, A. R., Wang, X., Wu, R., Zhang, Q.,
488   and Zhang, Y.: Measurements of traffic-dominated pollutant emissions in a Chinese
489   megacity, Atmos Chem Phys, 20, 8737-8761, 10.5194/acp-20-8737-2020, 2020.
490   Tang, X., Zhu, J., Wang, Z. F., Wang, M., Gbaguidi, A., Li, J., Shao, M., Tang, G. Q., and Ji,
491   D. S.: Inversion of CO emissions over Beijing and its surrounding areas with ensemble
492   Kalman filter, Atmos Environ, 81, 676-686, 10.1016/j.atmosenv.2013.08.051, 2013.
493   Todling, R., and Cohn, S. E.: Suboptimal schemes for atmospheric data assimilation based on
494   the   Kalman   filter,   Monthly   Weather   Review,   122,   10.1175/1520-
495   0493(1994)122<2530:SSFADA>2.0.CO;2, 1994.
496   Wang, Y., Gao, W., Wang, S., Song, T., Gong, Z., Ji, D., Wang, L., Liu, Z., Tang, G., Huo, Y.,
497   Tian, S., Li, J., Li, M., Yang, Y., Chu, B., Petäjä, T., Kerminen, V.-M., He, H., Hao, J.,
498   Kulmala, M., Wang, Y., and Zhang, Y.: Contrasting trends of $PM_{2.5}$ and surface-ozone
499   concentrations   in   China   from   2013   to   2017,   Natl   Sci   Rev,   7,   1331-1339,
500   10.1093/nsr/nwaa032, 2020.
501   Worden, H. M., Deeter, M. N., Edwards, D. P., Gille, J. C., Drummond, J. R., and Nédélec, P.:
502   Observations of near-surface carbon monoxide from space using MOPITT multispectral
503   retrievals, Journal of Geophysical Research, 115, 10.1029/2010jd014242, 2010.
504   Zheng, B., Chevallier, F., Ciais, P., Yin, Y., Deeter, M. N., Worden, H. M., Wang, Y., Zhang,
505   Q., and He, K.: Rapid decline in carbon monoxide emissions and export from East Asia
506   between years 2005 and 2016, Environ Res Let, 13, 10.1088/1748-9326/aab2b3, 2018a.
507   Zheng, B., Tong, D., Li, M., Liu, F., Hong, C., Geng, G., Li, H., Li, X., Peng, L., Qi, J., Yan,
508   L., Zhang, Y., Zhao, H., Zheng, Y., He, K., and Zhang, Q.: Trends in China's anthropogenic
509   emissions since 2010 as the consequence of clean air actions, Atmos Chem Phys, 18, 14095-
510   14111, 10.5194/acp-18-14095-2018, 2018b.
511

Surface CO Concentrations (ppb or ppb/y)		E. China		NCP		YRD		South Korea		Japan	
		Mean	Trend	Mean	Trend	Mean	Trend	Mean	Trend	Mean	Trend
CO observations	surface CO of MOPITT	222.9	-0.95	338.3	-6.29	356.3	0.26	254.6	-1.58	168.1	-0.21
a priori simulation	surface CO	267.8	-0.57	444.8	-2.60	417.6	-6.13	173.5	-1.78	150.5	-1.68
Kalman Filter assimilations by assimilating:	MOPITT CO profile (10 levels)	295.8	-1.40	479.9	-4.11	446.6	-6.98	204.5	-2.59	175.5	-2.54
	MOPITT CO column	289.2	-0.74	469.2	-2.82	438.1	-6.23	195.5	-2.08	170.6	-1.96
	MEE CO	429.8	-18.31	630.1	-43.92	598.4	-19.17	236.3	-8.37	183.5	-5.51
	MEE CO (normalized)	283.7	-10.79	505.0	-32.47	418.0	-14.69	186.5	-5.30	157.2	-3.59
	MEE CO morning data (normalized)	270.8	-6.67	462.8	-22.13	412.2	-10.02	177.5	-3.92	152.4	-2.80
	MEE CO (normalized) + MOPITT profile	290.6	-10.28	511.4	-32.10	421.1	-14.41	195.8	-4.37	166.0	-2.40
CO Columns (1×10^{18} molec/cm^2 or 1×10^{18} molec/cm^2/y)		E. China		NCP		YRD		South Korea		Japan	
		Mean	Trend	Mean	Trend	Mean	Trend	Mean	Trend	Mean	Trend
CO observations	Column CO of MOPITT	2.17	-0.017	2.61	-0.042	2.83	-0.017	2.46	-0.020	2.30	-0.015
a priori simulation	Column CO	1.86	-0.014	2.33	-0.021	2.57	-0.014	1.97	-0.019	1.87	-0.020
Kalman Filter assimilations by assimilating:	MOPITT CO profile (10 levels)	2.35	-0.017	2.89	-0.023	3.11	-0.017	2.50	-0.021	2.37	-0.021
	MOPITT CO column	2.25	-0.021	2.79	-0.029	2.98	-0.020	2.40	-0.027	2.27	-0.026
	MEE CO	2.35	-0.061	3.16	-0.139	3.53	-0.089	2.46	-0.068	2.25	-0.058
	MEE CO (normalized)	1.93	-0.040	2.57	-0.091	2.75	-0.060	2.07	-0.045	1.94	-0.040
	MEE CO morning data (normalized)	2.07	-0.041	2.75	-0.093	2.90	-0.060	2.24	-0.046	2.10	-0.040
	MEE CO (normalized) + MOPITT column	2.07	-0.041	2.75	-0.093	2.90	-0.060	2.24	-0.046	2.10	-0.040

Table. 1. Averages and trends of surface and column CO concentrations in 2015-2020. The domain definitions are shown in Fig. 1a.

Surface CO Concentrations sampled at MEE locations (ppb or ppb/y)		E. China		NCP		YRD	
		Mean	Trend	Mean	Trend	Mean	Trend
CO observations	surface CO of MOPITT	317.1	-2.05	384.5	-8.83	375.7	-0.66
	MEE CO	781.4	-43.55	880.6	-79.85	700.1	-23.34
a priori simulation	surface CO	397.0	-1.07	602.7	-1.66	479.6	-7.43
Kalman Filter assimilations by assimilating:	MOPITT CO profile (10 levels)	426.5	-2.12	639.0	-3.40	508.8	-8.25
	MOPITT CO column	417.9	-1.21	627.0	-1.88	500.1	-7.53
	MEE CO	631.2	-30.58	805.9	-62.24	656.7	-21.01
	MEE CO (normalized)	410.3	-18.61	677.9	-50.96	463.0	-18.23
	MEE CO morning data (normalized)	398.4	-12.55	623.8	-32.77	469.2	-13.58
	MEE CO (normalized) + MOPITT profile	414.1	-18.24	681.7	-50.71	465.3	-18.01
CO Columns Sampled at MEE locations (1×10^{18} molec/cm^2 or 1×10^{18} molec/cm^2/y)		E. China		NCP		YRD	
		Mean	Trend	Mean	Trend	Mean	Trend
CO observations	Column CO of MOPITT	2.63	-0.051	2.87	-0.117	2.92	-0.026
a priori simulation	Column CO	2.40	-0.011	2.67	-0.021	2.68	-0.013
Kalman Filter assimilations by assimilating:	MOPITT CO profile (10 levels)	2.93	-0.015	3.25	-0.024	3.22	-0.017
	MOPITT CO column	2.80	-0.018	3.14	-0.029	3.09	-0.020
	MEE CO	3.29	-0.101	3.63	-0.170	3.68	-0.089
	MEE CO (normalized)	2.55	-0.063	2.97	-0.115	2.87	-0.063
	MEE CO morning data (normalized)	2.44	-0.043	2.76	-0.083	2.72	-0.040
	MEE CO (normalized) + MOPITT column	2.70	-0.064	3.16	-0.117	3.01	-0.063

Table. 2. Averages and trends of surface and column CO concentrations in 2015-2020, sampled at the locations of MEE stations. The domain definitions are shown in Fig. 1a.
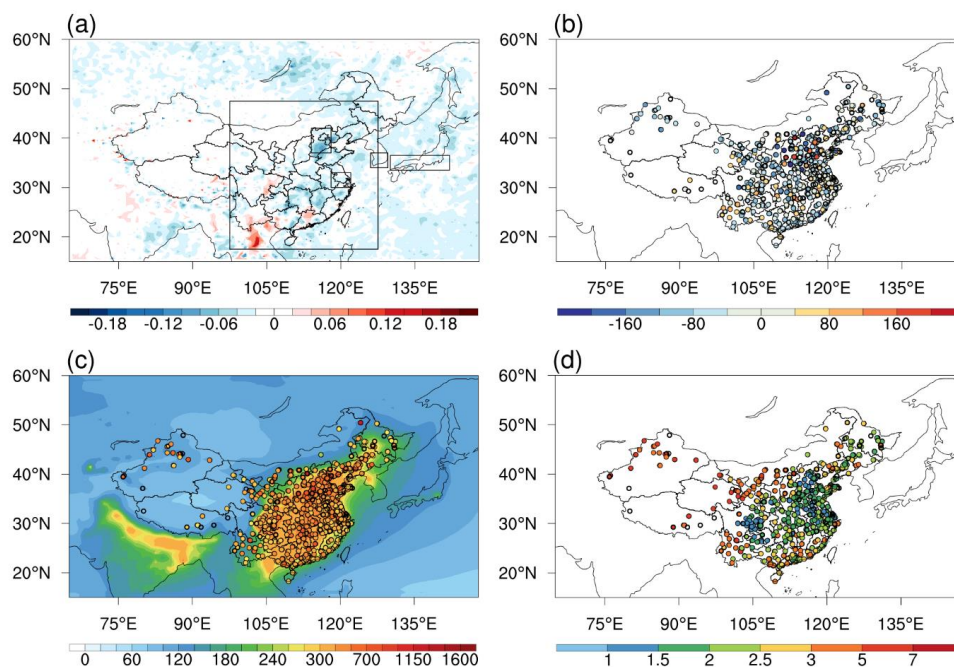
Fig. 1. (A) Trends of MOPITT CO columns in 2015-2020 with unit 10^{18} molec/cm^2/y; (B) Trends of MEE surface CO concentrations in 2015-2020 with unit ppb/y; (C) Modeled (contour) and observed (dotted) surface CO concentrations in 2019 with unit ppb; (D) Ratios between observed and modeled surface CO concentrations in 2019. The black boxes in panel A define the domains (land only) of E. China, NCP, YRD, South Korea and Japan. The areas outside of China are excluded in the E. China domain.
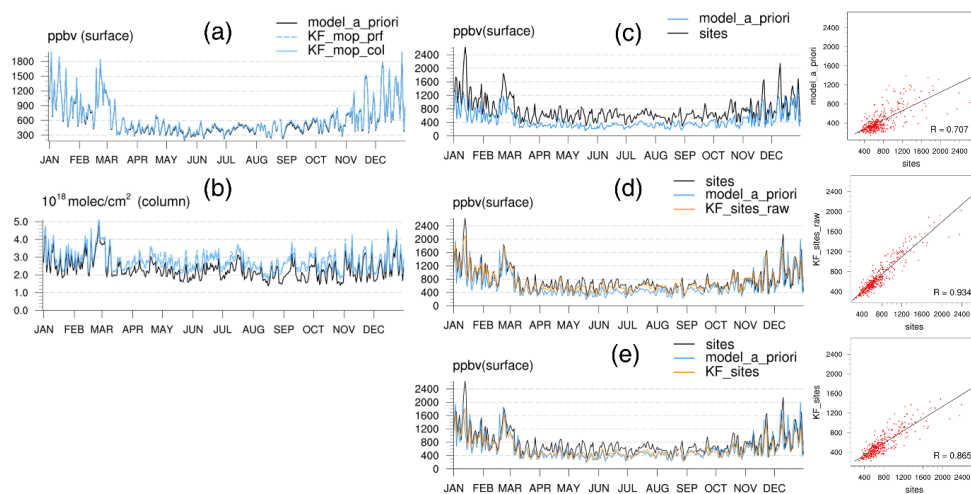
Fig. 2. (A) surface CO concentrations over NCP in 2019 from a priori simulation and Kalman Filter by assimilating MOPITT CO; (B) same as panel a, but for CO columns; (C) surface CO concentrations from a priori simulation and MEE observations; (D) surface CO concentrations from a priori simulation, MEE observations and Kalman Filter by assimilating MEE CO; (E) surface CO concentrations from a priori simulation, MEE observations and Kalman Filter by assimilating normalized MEE CO.
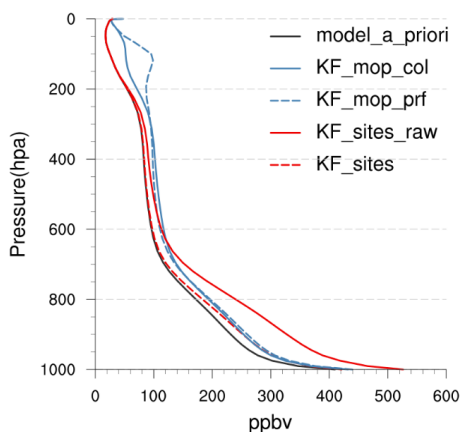
Fig. 3. CO profiles over NCP in 2019 from a priori simulations (black line), Kalman Filter by assimilating MOPITT CO (column: blue solid line; profile: blue dashed line) and MEE CO (raw data: red solid line; normalized data: red dashed line).
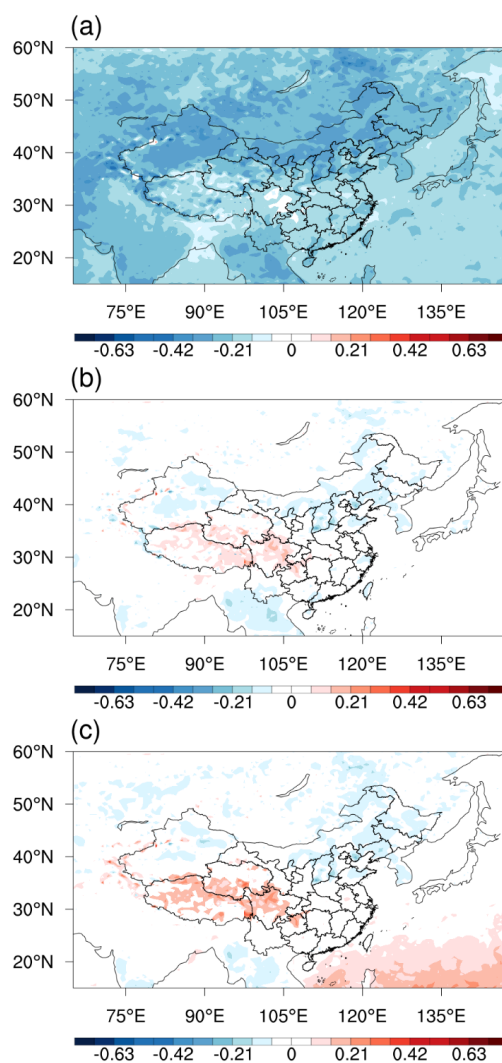
Fig. 4. (A) relative difference between a priori simulation and MOPITT in 2019, calculated by (Model - MOPITT)/MOPITT; (B) same as panel A, but with Kalman Filter by assimilating MOPITT CO column data; (C) same as panel A, but with Kalman Filter by assimilating MOPITT CO profile data.
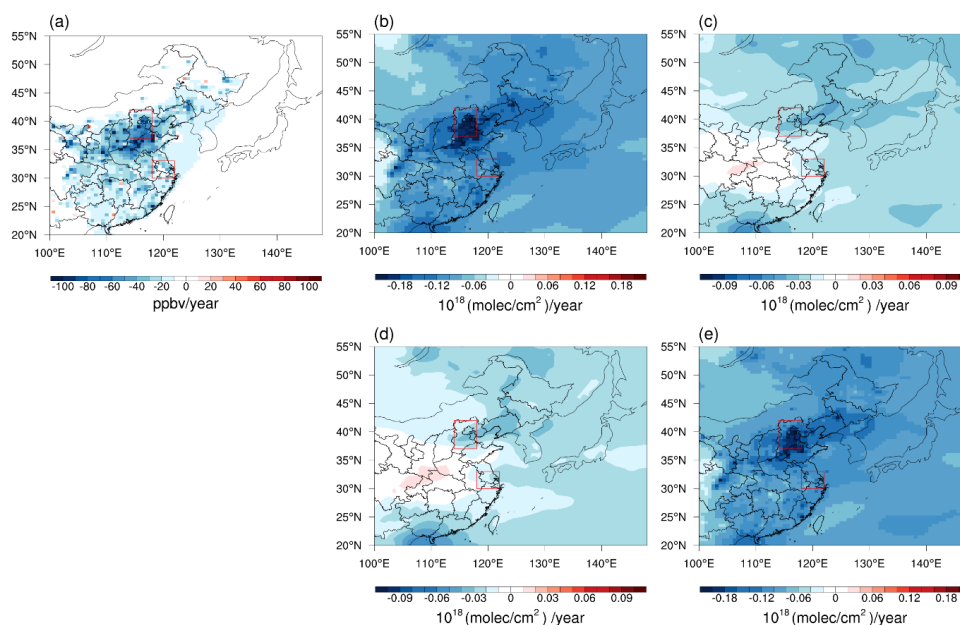
Fig. 5. Trends of surface CO concentrations in 2015-2020 by assimilating raw MEE CO (A) and trends of CO columns in 2015-2020 by assimilating (B) normalized MEE CO; (C) MOPITT CO column data; (D) MOPITT CO profile data; (E) normalized MEE CO + MOPITT CO column data.
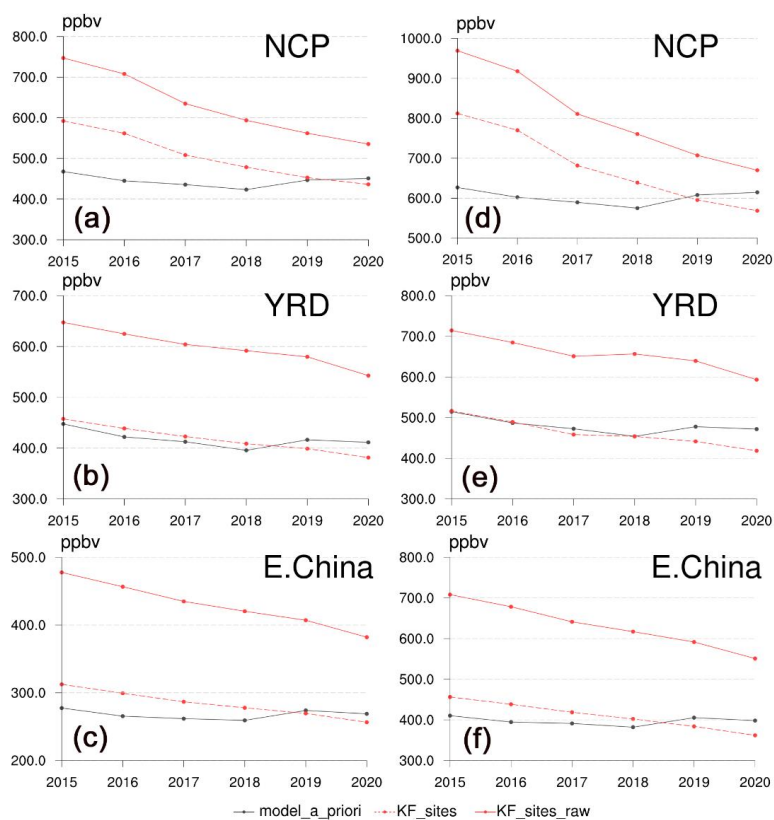
Fig. 6. (A-C) Surface CO concentrations in 2015-2019 from a priori simulations (black line), Kalman Filter by assimilating raw (red solid line) and normalized (red dashed line) MEE CO. (D-F) same as panels a-c, but sampled at the locations of MEE stations.
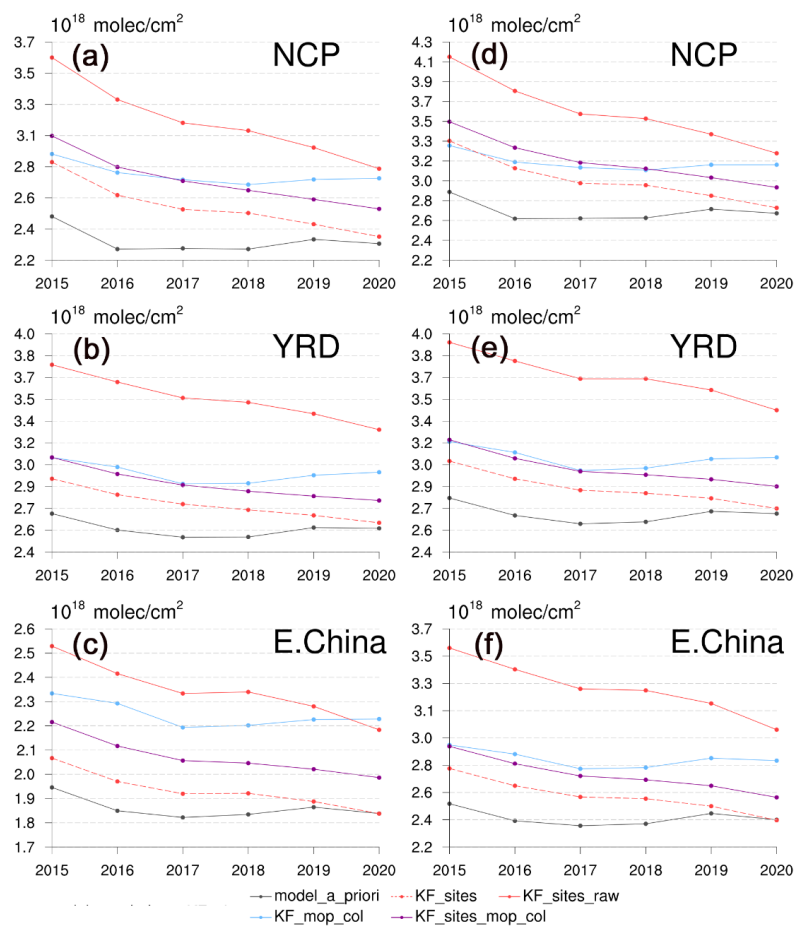
Fig. 7. (A-C) CO columns in 2015-2020 from a priori simulations (black line), Kalman Filter by assimilating MOPITT CO columns (blue line), MEE CO (raw data: red solid line; normalized data: red dashed line) and MOPITT CO column + normalized MEE CO (purple line). (D-F) same as panels a-c, but sampled at the locations of MEE stations.